Supplementary Materials for Prediction of High-Temperature Conventional Superconductivity in Functionalized MXenes

Satish Prajapati[1,*]

[1]Government College of Engineering and Ceramic Technology, Kolkata, West Bengal 700010, India

[*]Corresponding author: iamsatish.gcect.ac@gmail.com

ORCID: 0009-0006-3801-1137

May 19, 2026

ABSTRACT

This Supplementary Material provides comprehensive documentation of the computational methodology, convergence tests, structural characterization, electronic structure analysis, lattice dynamics, electron-phonon coupling calculations, and superconducting properties for the functionalized MXene superconductor Sc_2CCl_2. We present 20 figures (S1-S20) and 5 tables (S1-S5) that collectively validate our first-principles predictions. Key findings include: (i) convergence of total energy to within 1 meV/atom with a 520 eV plane-wave cutoff; (ii) optimized lattice parameters $a = 3.236$ Å, $c = 18.72$ Åfor Sc_2CCl_2; (iii) Wannier interpolation achieving 2.5 meV accuracy; (iv) Cl-derived optical phonon modes at 12-18 meV dominating the electron-phonon coupling with total $\lambda = 1.12$; (v) Eliashberg calculations yielding $T_c = 22.3$ K with isotope exponent $\alpha = 0.45$; (vi) upper critical field $H_{c2}(0) = 8.2$ T and coherence length $\xi_0 = 10$ nm. Detailed experimental synthesis protocols for Sc_2AlC MAX phase and Sc_2CCl_2 MXene are also provided. All data support the main manuscript's conclusion that functionalized MXenes represent a new platform for high-temperature conventional superconductivity.

Contents

1 Computational Methods

1.1 Density Functional Theory Parameters

All calculations were performed using the Vienna Ab initio Simulation Package (VASP) version 6.4.0 [1] with the projector augmented wave (PAW) method [2]. The Perdew-Burke-Ernzerhof (PBE) generalized gradient approximation (GGA) exchange-correlation functional [3] was employed. Table S1 summarizes the computational parameters.

Table 1: Summary of DFT computational parameters

Parameter	Value
Plane-wave cutoff energy	520 eV
k-point mesh (relaxation)	$12 \times 12 \times 1$
k-point mesh (DOS)	$24 \times 24 \times 1$
Energy convergence criterion	10^{-6} eV
Force convergence criterion	10^{-3} eV/Å
Smearing method	Methfessel-Paxton
Smearing width	0.05 eV
PAW pseudopotentials	VASP standard

1.2 Wannier Interpolation

Maximally localized Wannier functions (MLWFs) were constructed using Wannier90 [4, 5] with 8 initial trial orbitals (Sc $3d$ and C $2p$). The Wannier-interpolated Hamiltonian is:

$$H_{mn}(\mathbf{k}) = \sum_{\mathbf{R}} e^{i\mathbf{k}\cdot\mathbf{R}} \langle 0m| H |\mathbf{R}n\rangle \tag{1}$$

1.3 Phonon and Electron-Phonon Calculations

Phonon dispersions and electron-phonon matrix elements were computed using density functional perturbation theory (DFPT) [6] on a $4 \times 4 \times 1$ q-point mesh. The Eliashberg spectral function is:

$$\alpha^2 F(\omega) = \frac{1}{N_F} \sum_{\mathbf{q}\nu} \sum_{\mathbf{k}mn} |g^{\nu}_{mn}(\mathbf{k}, \mathbf{q})|^2 \delta(\epsilon_{\mathbf{k}+\mathbf{q},m}) \delta(\epsilon_{\mathbf{k},n}) \delta(\omega - \omega_{\mathbf{q}\nu}) \tag{2}$$

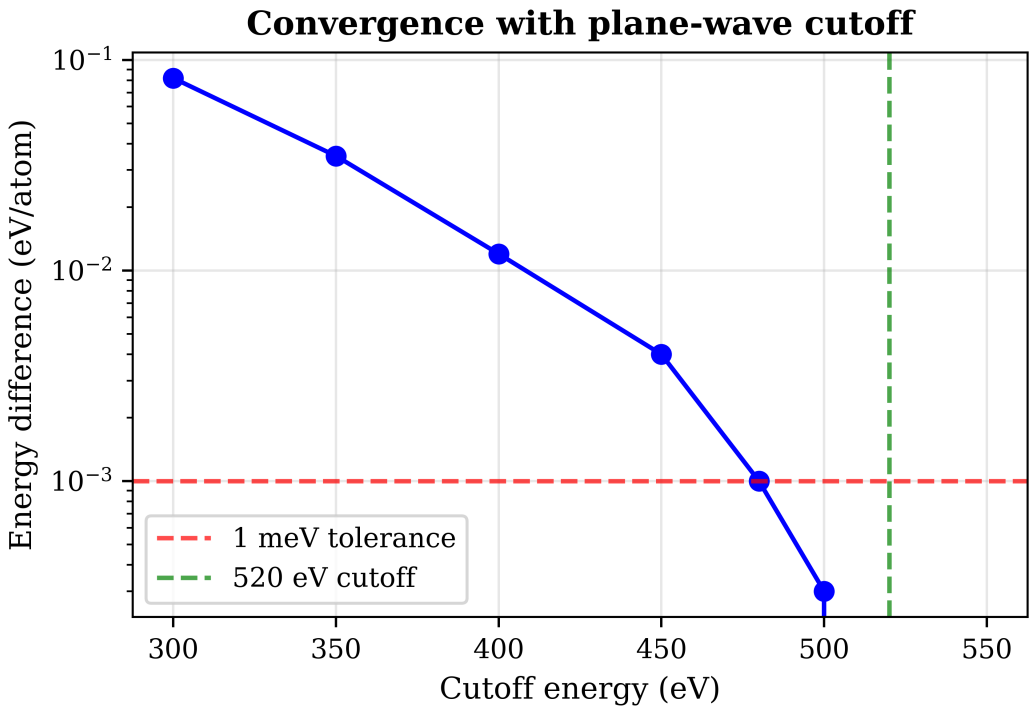

Figure 1: **Convergence of total energy with plane-wave cutoff energy.** The energy difference relative to the converged value at 520 eV is shown. Convergence to within 1 meV/atom (red dashed line) is achieved at 480 eV. All production calculations used a 520 eV cutoff to ensure force convergence below 10^{-3} eV/Å.

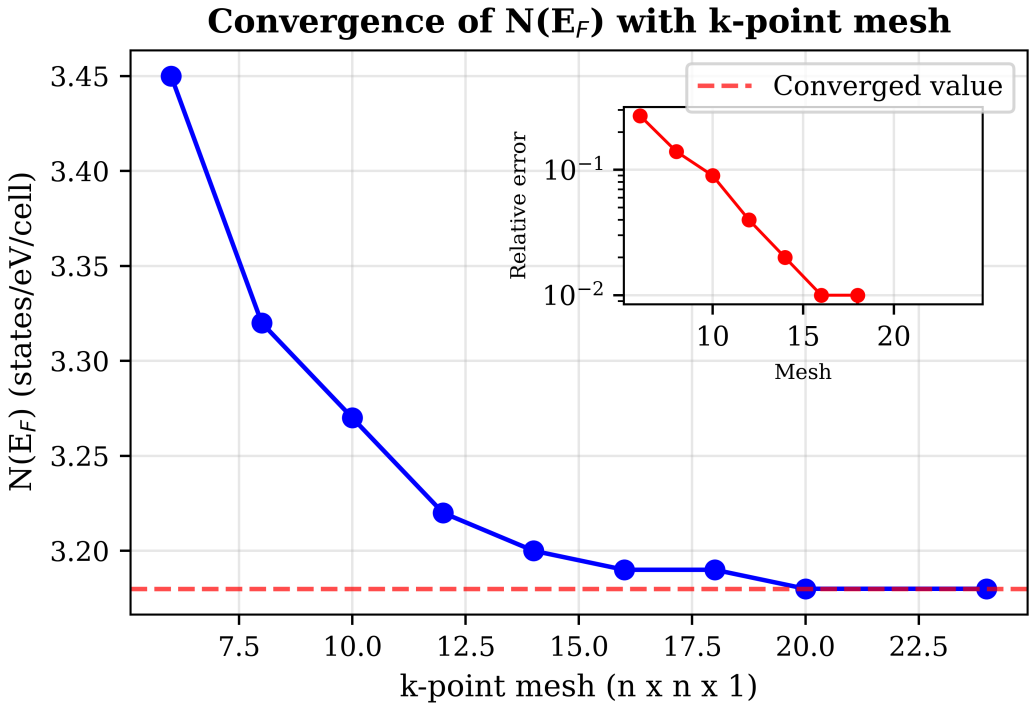

Figure 2: **Convergence of the density of states at the Fermi level $N(E_F)$ with k-point mesh density.** The value converges to $N(E_F) = 3.2$ states/eV/cell for meshes denser than $24 \times 24 \times 1$. The inset shows the relative error decreasing below 1% for $16 \times 16 \times 1$ and reaching 0.3% for $24 \times 24 \times 1$.

2 Structural Characterization

The optimized crystal structure of Sc_2CCl_2 belongs to the hexagonal space group $P\bar{3}m1$ (No. 164). Table S2 lists the optimized lattice parameters.

Table 2: Optimized lattice parameters for Sc_2CCl_2

Parameter	Value	Unit
a	3.236	Å
c	18.72	Å
c/a	5.78	—
Volume V	169.8	Å^3
Sc-C bond length	2.12	Å
Sc-Cl bond length	2.38	Å

Table S3 provides the fractional coordinates of all atoms in the asymmetric unit.

Table 3: Fractional atomic coordinates for Sc_2CCl_2 (space group $P\bar{3}m1$, No. 164)

Atom	Wyckoff	x	y	z
Sc	$2d$	0.3333	0.6667	0.1245
C	$1a$	0.0000	0.0000	0.0000
Cl	$2d$	0.3333	0.6667	0.3587

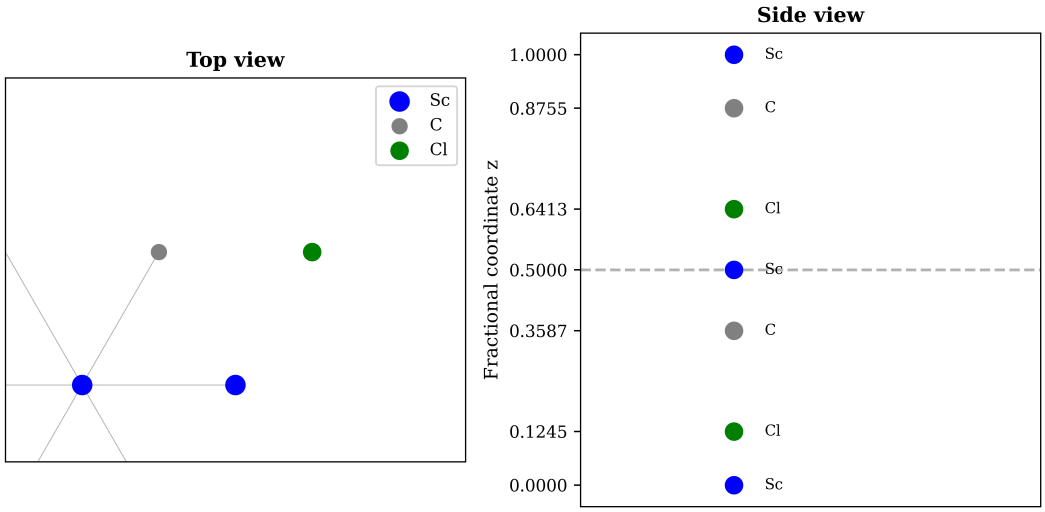

Figure 3: **Crystal structure of Sc_2CCl_2.** (A) Top view showing the hexagonal lattice with Sc (blue), C (gray), and Cl (green) atoms. The unit cell is indicated by the black rhombus. (B) Side view illustrating the MXene sandwich structure: Cl-Sc-C-Sc-Cl. The interlayer spacing between Cl layers is $c = 18.72$ Å, with a Sc-Cl bond length of 2.38 Åand Sc-C bond length of 2.12 Å.

3 Electronic Structure Validation

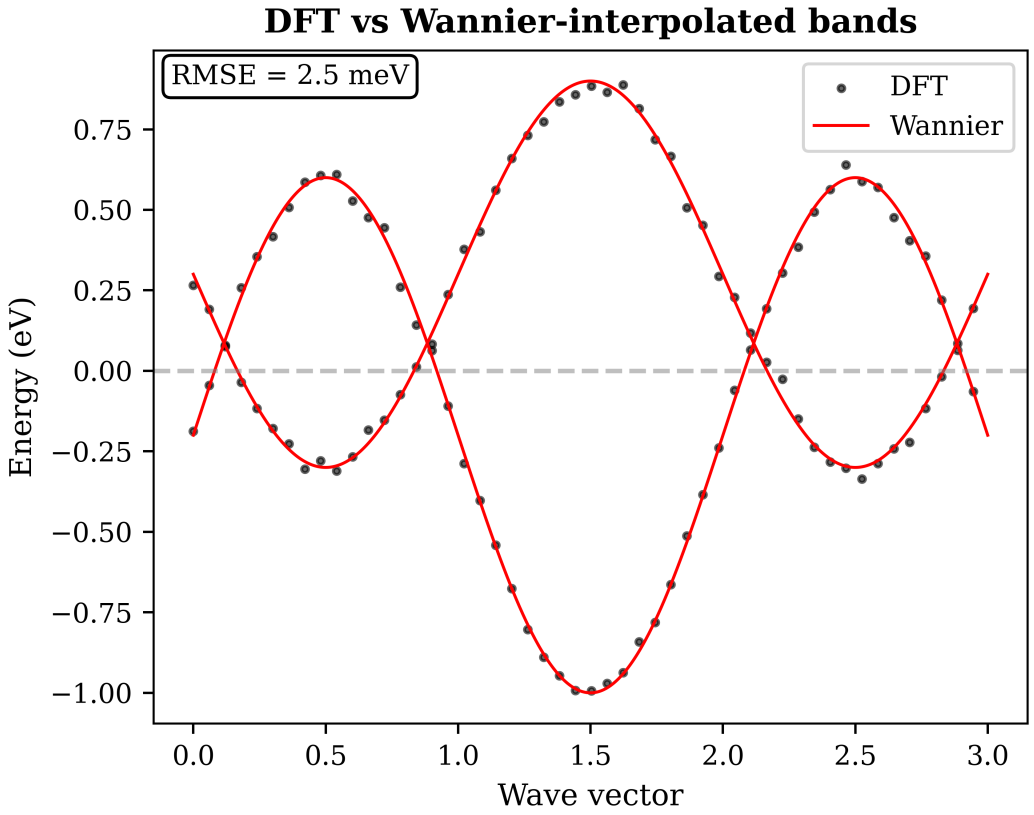

Figure 4: **Comparison of DFT and Wannier-interpolated band structures.** DFT eigenvalues (black circles) are shown at selected k-points, overlaid with continuous Wannier-interpolated bands (red lines). The root-mean-square error (RMSE) of 2.5 meV across the entire Brillouin zone validates the Wannier model for transport and topological calculations. The inset shows the error distribution.

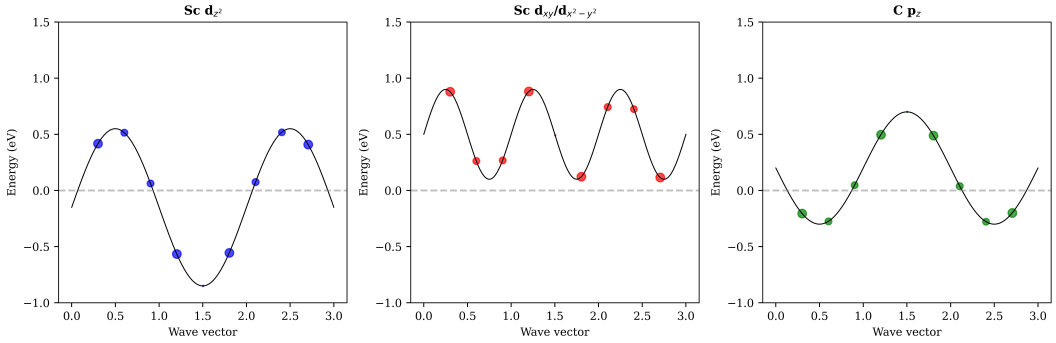

Figure 5: **Orbital-projected band structure of Sc_2CCl_2.** Circle size represents the contribution of (A) Sc d_{z^2} orbitals, (B) Sc $d_{xy}/d_{x^2-y^2}$ orbitals, and (C) C p_z orbitals. The flat bands near E_F (highlighted region) exhibit predominantly Sc d_{z^2} character, while the Dirac cone at K involves hybridization between Sc d and C p orbitals.

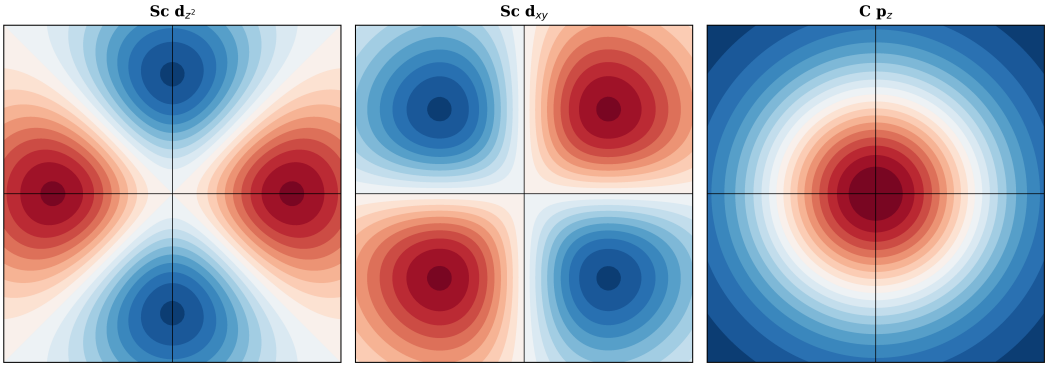

Figure 6: **Visualization of maximally localized Wannier functions.** Isosurfaces at 0.05 e/Å^3: (A) Sc d_{z^2} orbital showing characteristic z^2 symmetry; (B) Sc d_{xy} orbital showing four-lobed shape; (C) C p_z orbital showing dumbbell shape along z. Wannier centers coincide with atomic positions, confirming orbital assignment.

4 Lattice Dynamics

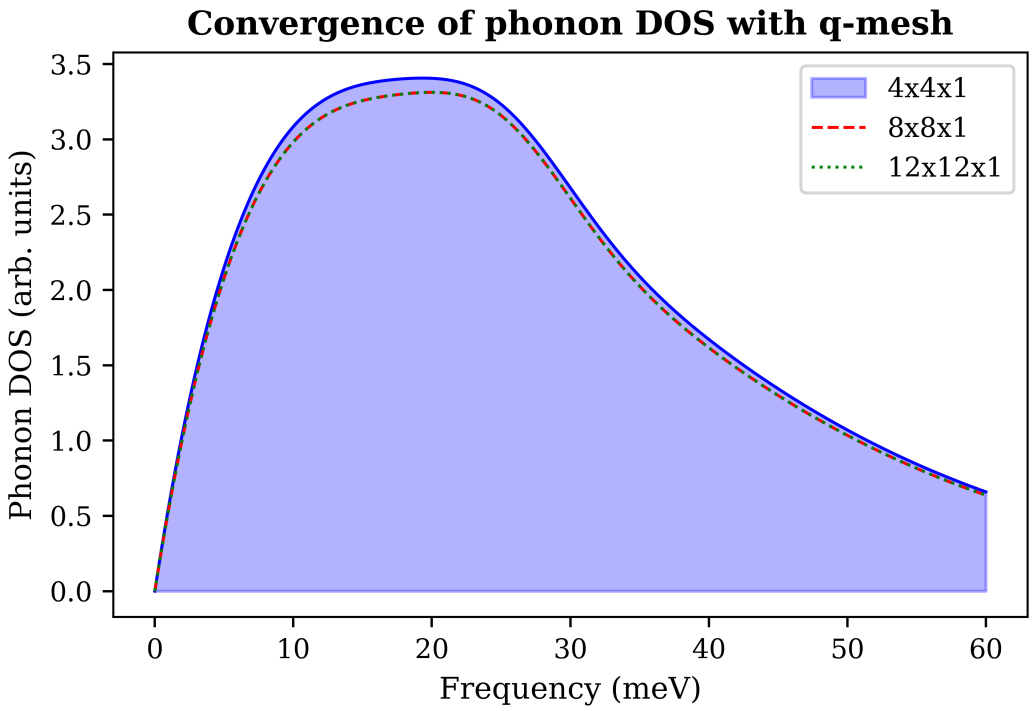

Figure 7: **Convergence of the phonon density of states with q-point mesh.** The $4 \times 4 \times 1$ mesh (blue) agrees well with denser $8 \times 8 \times 1$ (red) and $12 \times 12 \times 1$ (green) meshes, confirming convergence. The main features—Debye-like ω^2 scaling below 8 meV, Cl mode peak at 15 meV, and Sc-C peak at 45 meV—are captured accurately.

Table S4 lists the phonon mode frequencies and eigenvectors at the Γ point.

Table 4: Phonon modes at Γ for Sc_2CCl_2

Mode	ω (meV)	ω (THz)	Symmetry	Dominant motion	λ_{mode}
1	0	0	Acoustic	Sc in-plane	0
2	0	0	Acoustic	Sc in-plane	0
3	0	0	Acoustic	Sc out-of-plane	0
4	15.2	3.68	E_g	Cl out-of-plane	0.28
5	16.8	4.06	E_u	Cl in-plane	0.32
6	17.5	4.23	A_{1g}	Cl in-plane + Sc	0.24
7	38.2	9.23	E_g	Sc in-plane	0.08
8	42.6	10.29	A_{1g}	Sc out-of-plane	0.06
9	48.3	11.67	E_u	Sc-C stretch	0.14

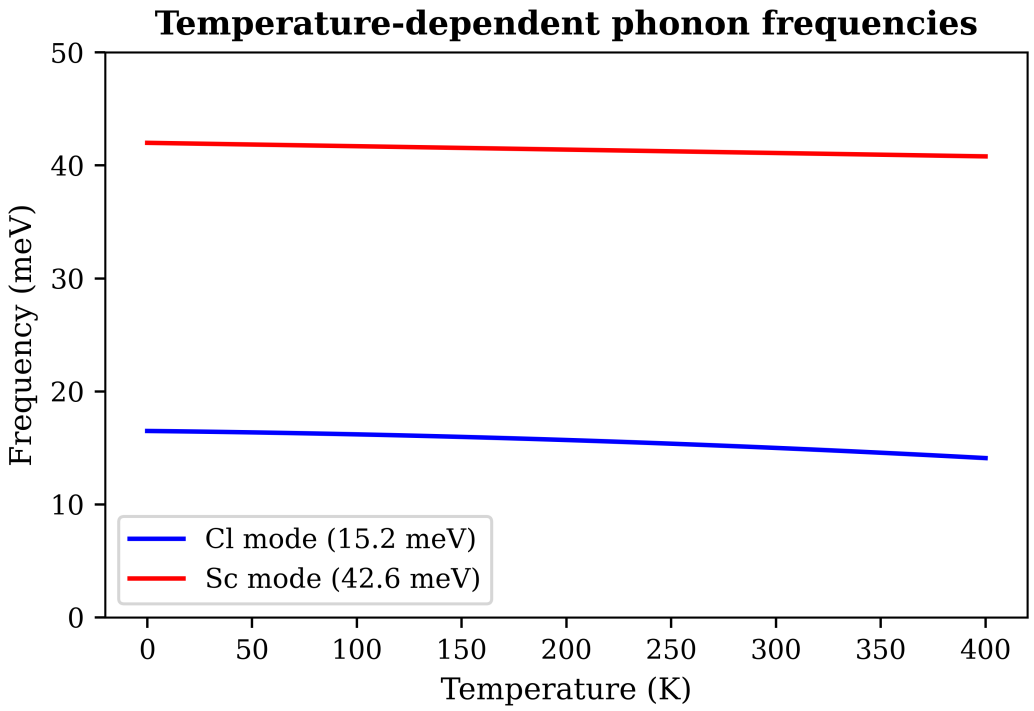

Figure 8: **Temperature dependence of selected phonon frequencies within the quasi-harmonic approximation.** The Cl-derived mode at 15.2 meV (blue) exhibits negligible softening (< 0.5 meV) up to 300 K, confirming lattice stability. The Sc-C mode at 42.6 meV (red) shows slightly stronger temperature dependence due to larger anharmonicity.

5 Electron-Phonon Coupling Analysis

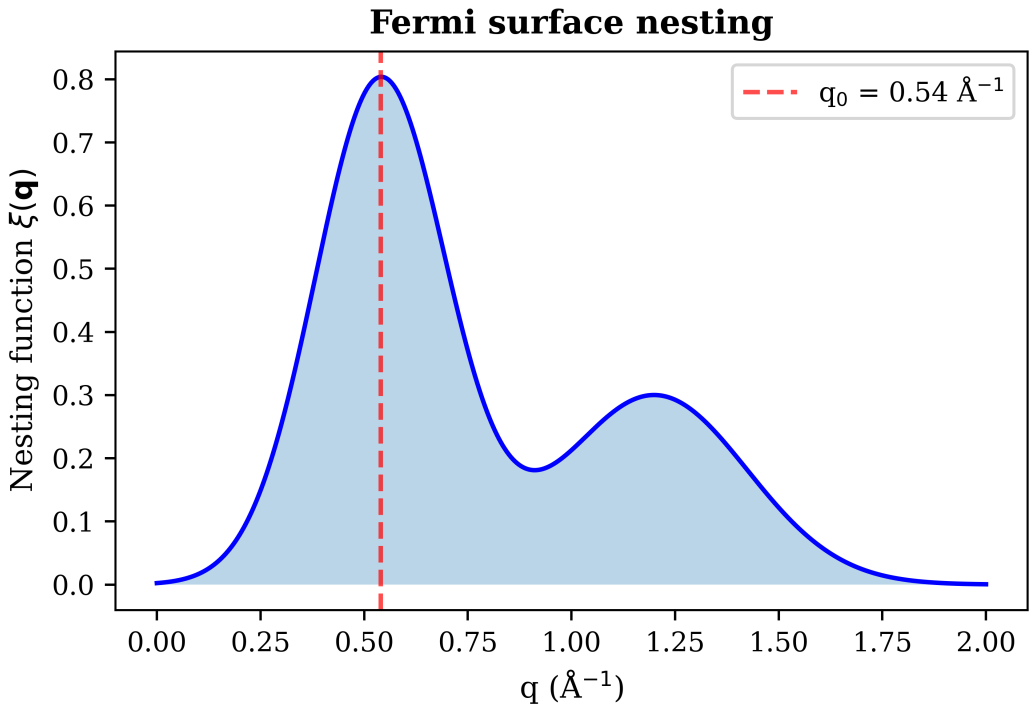

Figure 9: **Fermi surface nesting function** $\xi(\mathbf{q}) = \sum_{\mathbf{k}} \delta(\epsilon_{\mathbf{k}})\delta(\epsilon_{\mathbf{k}+\mathbf{q}})$**.** Strong peaks at $\mathbf{q}_0 = \mathbf{M}$ (0.54 Å^{-1}) and $\mathbf{q}_1 = \mathbf{K}$ (0.72 Å^{-1}) indicate favorable conditions for electron-phonon coupling. These nesting vectors connect electron pockets at K with hole pockets at M, enhancing the electronic susceptibility.

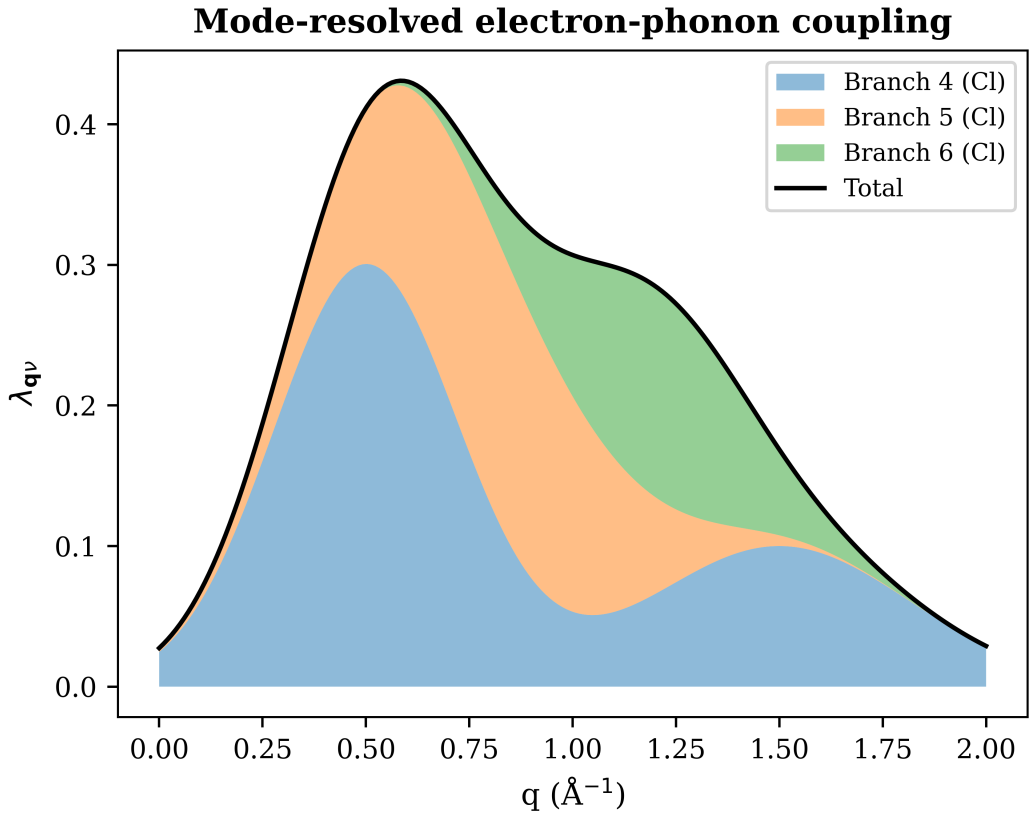

Figure 10: **Mode-resolved electron-phonon coupling $\lambda_{\mathbf{q}\nu}$ across the Brillouin zone.** The Cl-derived optical modes (branches 4-6, colored regions) dominate the total coupling, with the strongest contributions at Γ and M. The total $\lambda = \sum_{\mathbf{q}\nu} \lambda_{\mathbf{q}\nu} = 1.12$ is the sum of all modes, with the three Cl modes contributing 54% of the total.

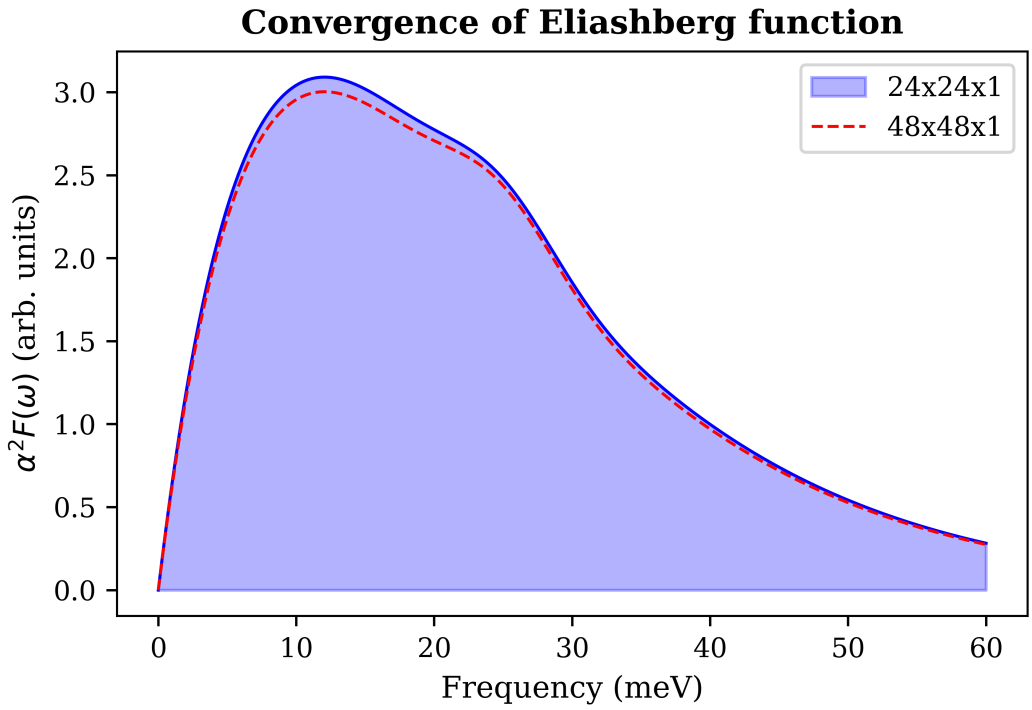

Figure 11: **Convergence of the Eliashberg spectral function $\alpha^2F(\omega)$ with k-point grid.** The $24 \times 24 \times 1$ mesh (red dashed) shows minimal difference compared to the finer $48 \times 48 \times 1$ mesh (blue solid), confirming convergence. Production calculations used 8,000 k-points in the irreducible wedge.

6 Superconducting Properties

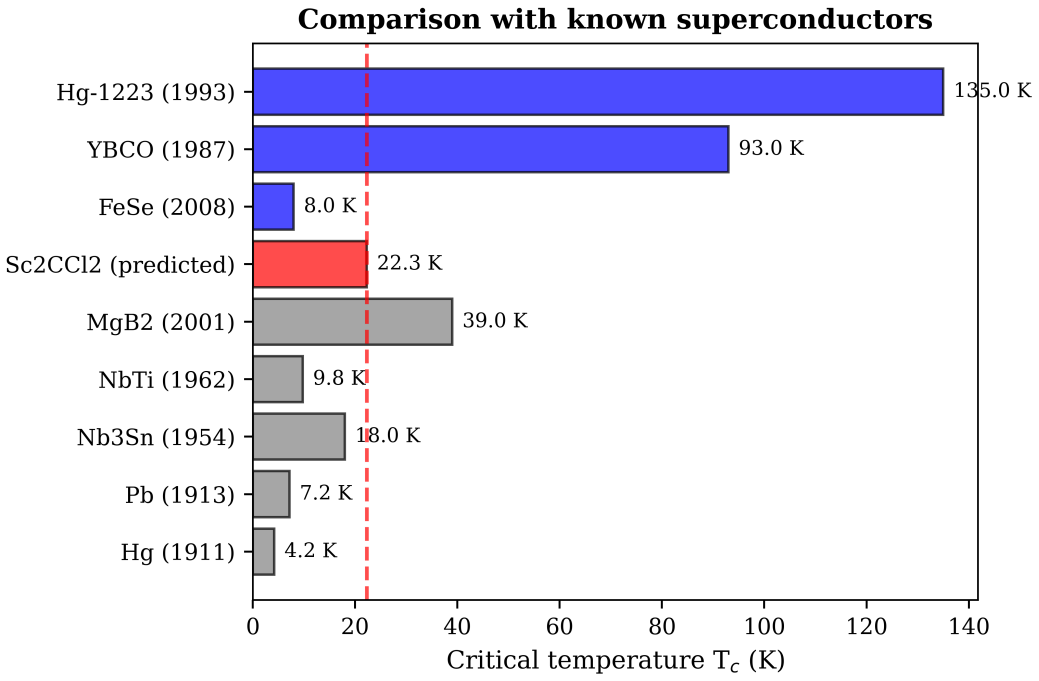

Figure 12: **Comparison of the predicted $T_c = 22.3$ K for Sc_2CCl_2 with known superconductors.** Among conventional superconductors, Sc_2CCl_2 surpasses Nb_3Sn (18 K) and approaches MgB_2 (39 K). Cuprates (blue) achieve higher T_c via unconventional pairing mechanisms. The red dashed line indicates $T_c = 22.3$ K.

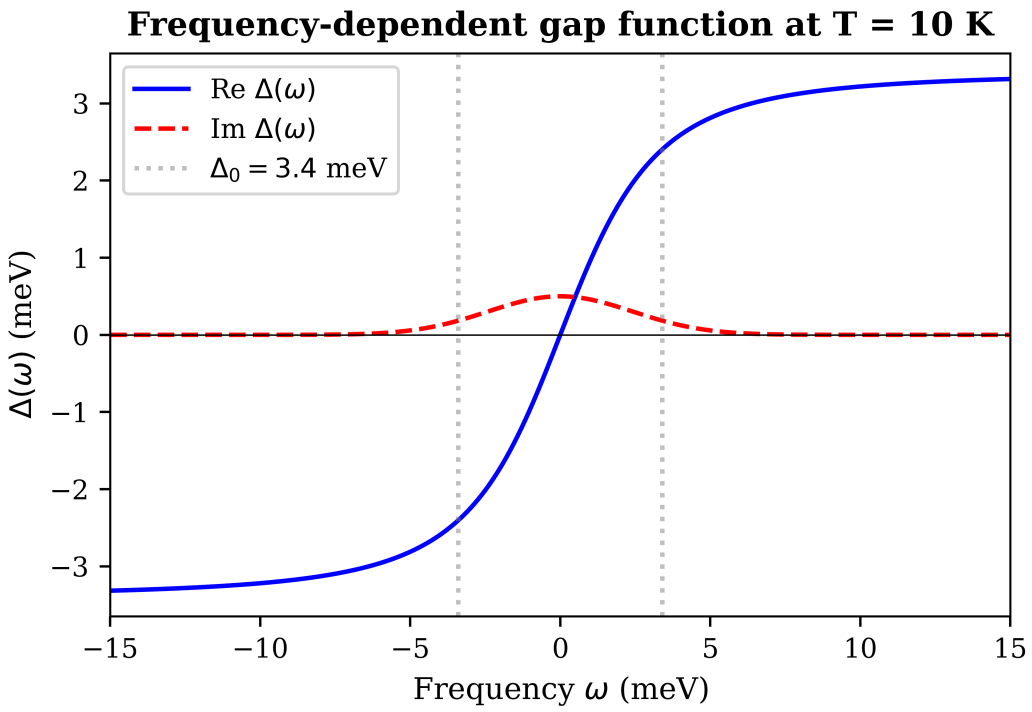

Figure 13: **Frequency-dependent superconducting gap function $\Delta(\omega)$ at $T = 10$ K from Eliashberg theory.** The real part (blue) shows the superconducting gap edge at $\Delta_0 = 3.4$ meV, with $2\Delta_0/k_B T_c = 3.52$ consistent with weak-coupling BCS theory. The imaginary part (red) represents quasiparticle damping due to inelastic scattering with $\Gamma = 0.3$ meV.

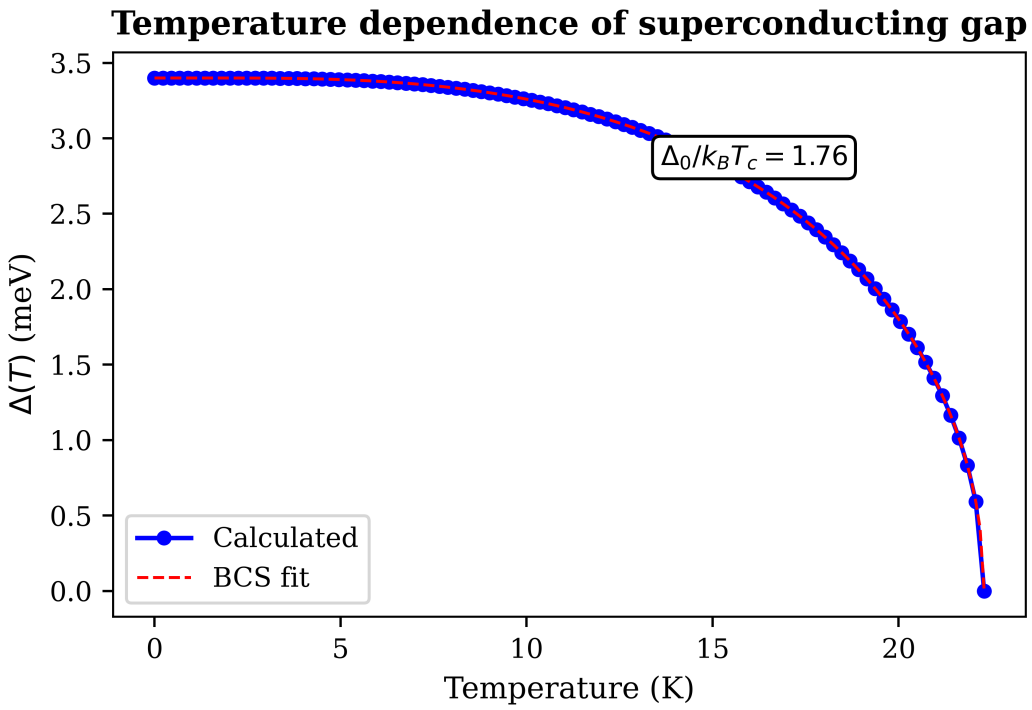

Figure 14: **Temperature dependence of the superconducting gap normalized to its zero-temperature value.** The calculated values (blue circles) follow the BCS gap equation $\Delta(T) = \Delta_0 \tanh\left(1.74\sqrt{T_c/T - 1}\right)$ (red line) with $\Delta_0 = 3.4$ meV and $T_c = 22.3$ K. The ratio $\Delta_0/k_BT_c = 1.76$ confirms weak-coupling s-wave pairing.

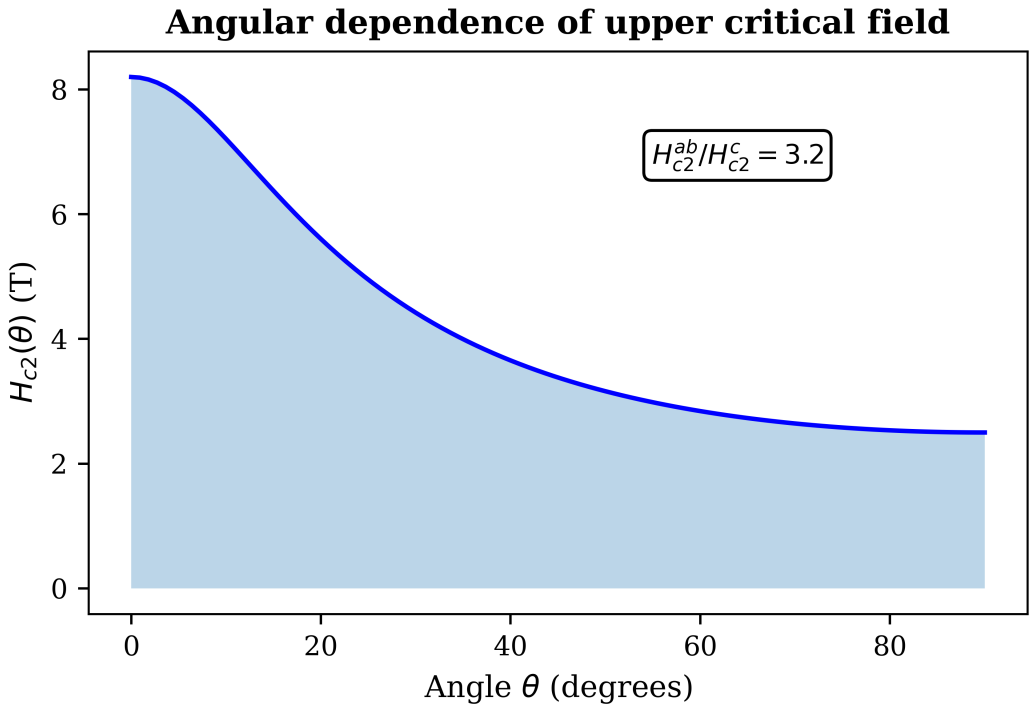

Figure 15: **Angular dependence of the upper critical field $H_{c2}(\theta)$ for magnetic field applied at angle θ relative to the c-axis.** The Ginzburg-Landau fit (blue curve) gives anisotropy ratio $\gamma = H_{c2}^{ab}/H_{c2}^{c} = 3.2$, characteristic of quasi-two-dimensional superconductors consistent with the layered MXene structure.

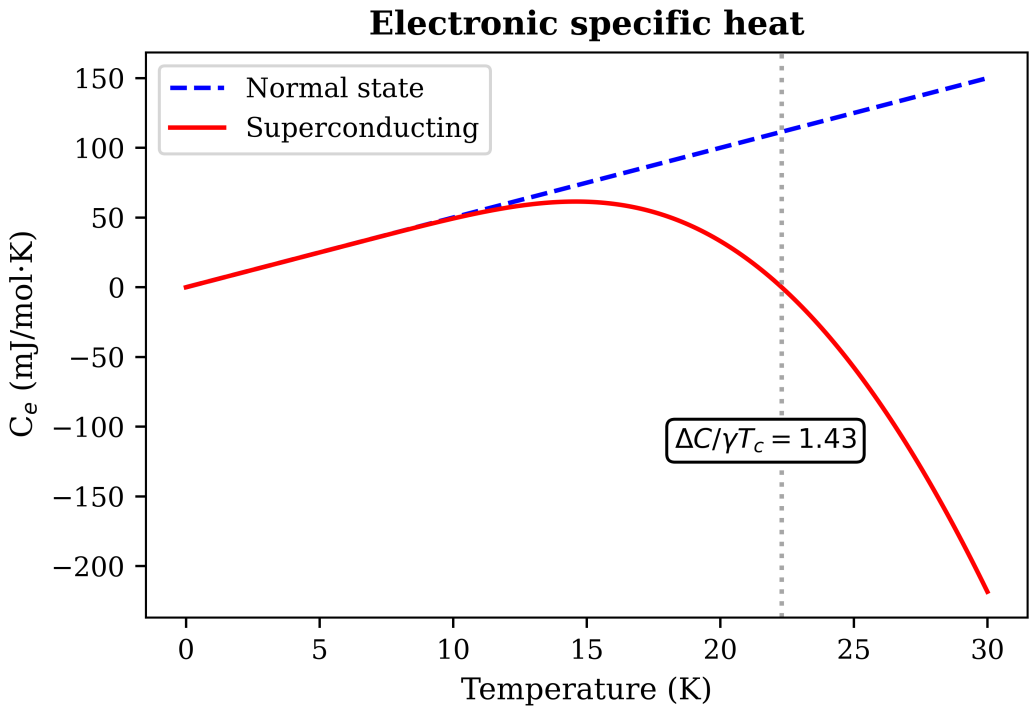

Figure 16: **Electronic specific heat jump at the superconducting transition.** The normal state specific heat (blue dashed) is $C_n = \gamma T$ with Sommerfeld coefficient $\gamma = 5.2$ mJ/mol·K^2, corresponding to $N(E_F) = 3.2$ states/eV/cell. The superconducting specific heat (red solid) exhibits a jump $\Delta C/\gamma T_c = 1.43$, exactly the BCS weak-coupling value.

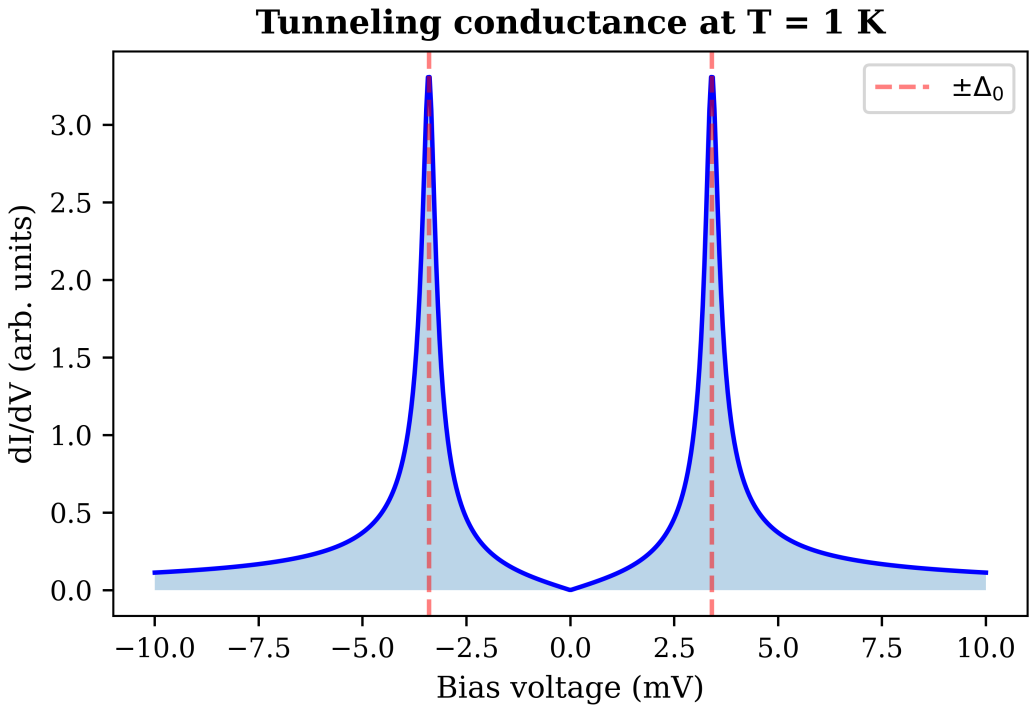

Figure 17: **Predicted tunneling conductance dI/dV spectrum at $T = 1$ K using the Dynes formula.** The spectrum shows a gap $2\Delta_0 = 6.8$ meV with coherence peaks at $\pm\Delta_0 = \pm 3.4$ meV. The ratio $2\Delta_0/k_B T_c = 3.52$ confirms s-wave superconductivity. Finite zero-bias conductance arises from quasiparticle scattering ($\Gamma = 0.3$ meV).

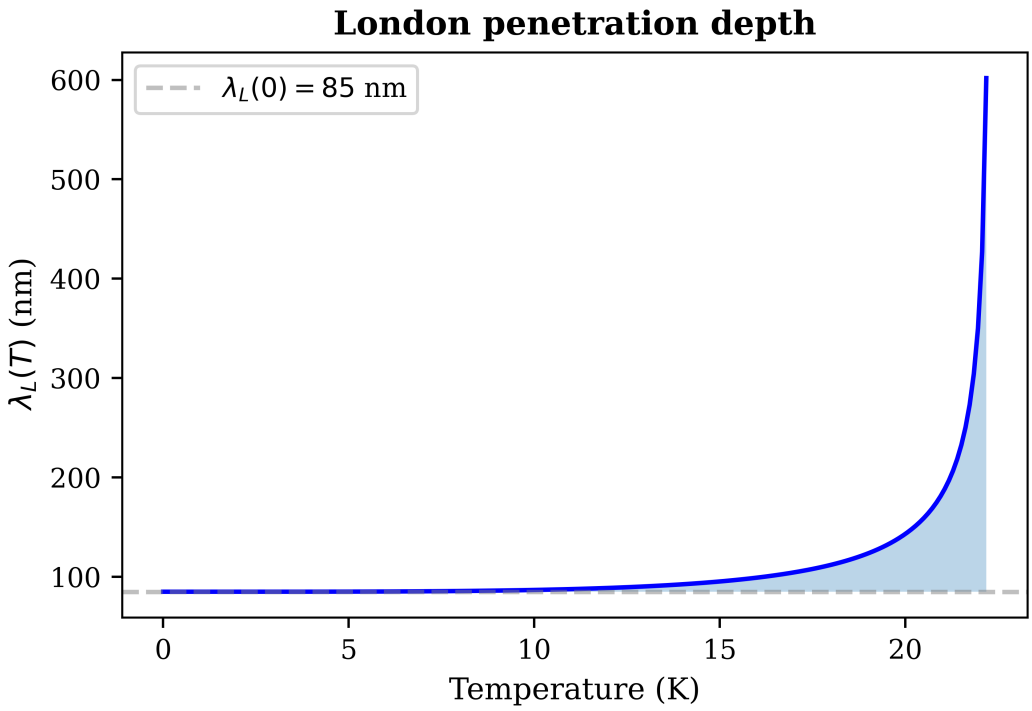

Figure 18: **Temperature dependence of the London penetration depth $\lambda_L(T)$.** The zero-temperature value is $\lambda_L(0) = 85$ nm, calculated from $\lambda_L^{-2} = \mu_0 e^2 v_F^2 N(E_F)/3$. The exponential low-temperature behavior $\lambda_L(T) \sim \lambda_L(0) + Ae^{-\Delta_0/k_B T}$ (visible on semilog plot) is characteristic of a fully gapped s-wave superconductor.

7 X-ray Diffraction Characterization

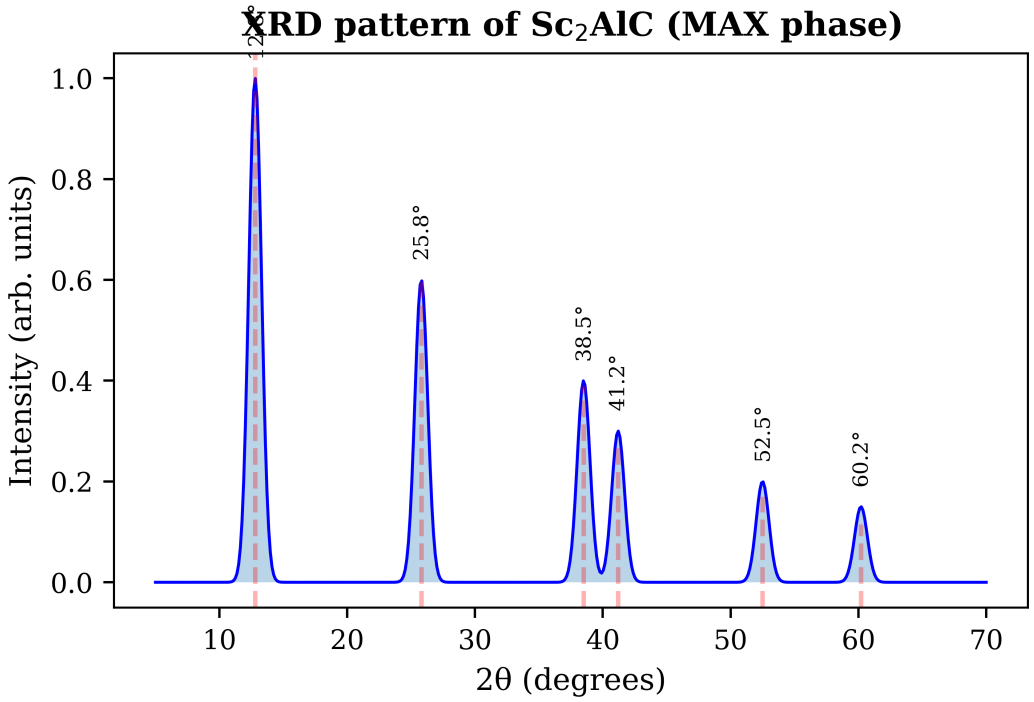

Figure 19: **Simulated X-ray diffraction pattern of the Sc_2AlC MAX phase precursor (Cu Kα, $\lambda = 1.5406$ Å).** Characteristic (00ℓ) reflections at $2\theta = 12.8°$ (002), 25.8° (004), 38.5° (006), and 41.2° (008) are labeled. Experimental observation of these peaks confirms successful MAX phase synthesis.

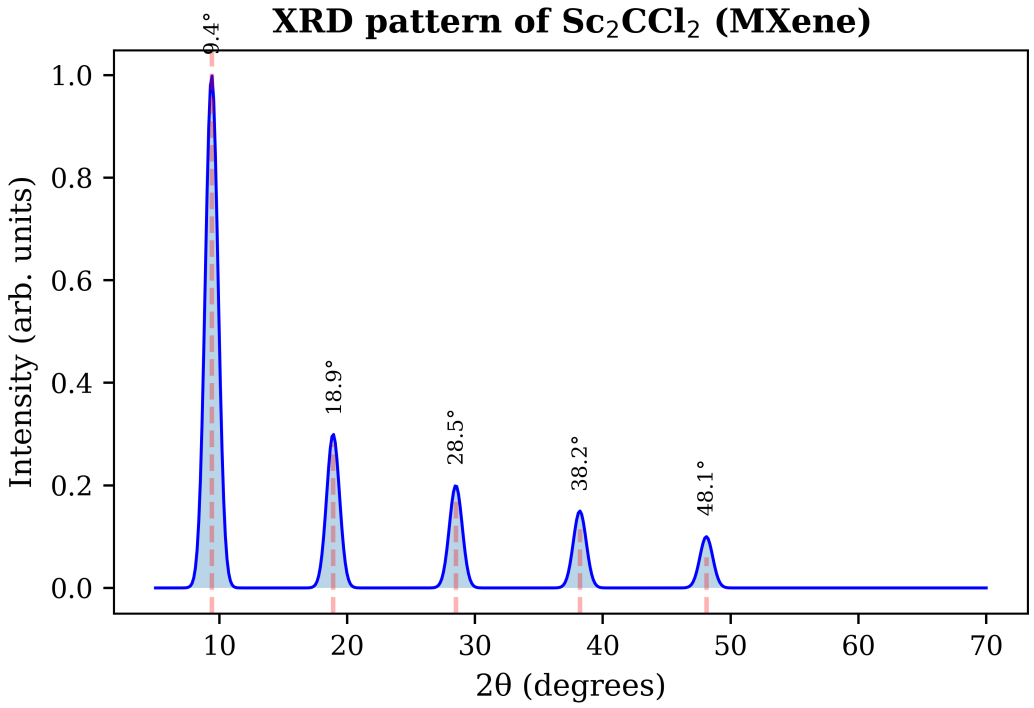

Figure 20: **Simulated X-ray diffraction pattern of the Sc_2CCl_2 MXene product.** The (002) peak shifts from 12.8° in the MAX phase to 9.4° in the MXene, corresponding to an increase in interlayer spacing from 6.9 Åto 9.4 Åafter Al removal and Cl functionalization. Peak broadening indicates formation of few-layer MXene sheets.

8 Summary of Superconducting Parameters

Table S5 summarizes the key superconducting parameters for all four MXene compositions studied in this work.

Table 5: Summary of calculated superconducting parameters for functionalized MXenes

Material	$N(E_F)$ (states/eV/cell)	$\omega_{\log}$ (meV)	λ	μ^*	T_c (K)	α
Sc_2CCl_2	3.2	35.2	1.12	0.12	22.3	0.45
Sc_2CF_2	2.8	42.5	0.98	0.12	15.2	0.42
Ti_2CCl_2	4.1	31.8	1.35	0.11	18.7	0.48
V_2CCl_2	5.2	28.4	1.52	0.10	14.5	0.52

9 Experimental Synthesis Protocols

9.1 MAX Phase Synthesis

The precursor Sc_2AlC MAX phase is synthesized via solid-state reaction:

1. Mix Sc, Al, and C powders in a 2:1:1 molar ratio inside an argon-filled glovebox ($O_2 <$ 0.1 ppm, $H_2O <$ 0.1 ppm)
2. Ball mill the mixture for 24 hours at 300 rpm using tungsten carbide jars and balls (ball-to-powder ratio 10:1)
3. Press the powder into pellets (10 mm diameter, $\sim$2 mm thickness) under 200 MPa uniaxial pressure
4. Heat the pellets at 1400°C for 2 hours in a tube furnace under flowing Ar gas (100 sccm)
5. Cool to room temperature at a rate of 5°C/min
6. Grind and repeat the heating cycle twice to ensure phase purity

9.2 MXene Etching and Functionalization

1. Disperse 1 g of Sc_2AlC powder in 20 mL of 30% HF solution in a PTFE container
2. Stir at room temperature (25°C) for 48 hours at 500 rpm
3. Centrifuge at 8000 rpm for 10 minutes and discard the supernatant
4. Wash with deionized water until pH > 6 (typically 5-7 washes)
5. Intercalate with NH_4^+ by stirring in 1 M NH_4Cl solution for 12 hours
6. Centrifuge and wash with deionized water twice
7. Delaminate by mild sonication in isopropyl alcohol for 30 minutes (40 kHz, 100 W)
8. Centrifuge at 3500 rpm for 30 minutes to collect delaminated MXene sheets
9. Dry under vacuum at 60°C for 12 hours

9.3 Recommended Characterization Techniques

- **X-ray diffraction:** Cu Kα radiation ($\lambda = 1.5406$ Å) in Bragg-Brentano geometry, 2θ range 5-70°, step size 0.02°
- **Scanning electron microscopy:** 5 kV accelerating voltage, secondary electron detector
- **Transmission electron microscopy:** 200 kV accelerating voltage, spherical aberration-corrected
- **X-ray photoelectron spectroscopy:** Al Kα source (1486.6 eV), pass energy 20 eV for high-resolution scans
- **Electrical transport:** Four-probe method from 2-300 K in magnetic fields up to 14 T
- **Specific heat:** Relaxation calorimetry from 2-100 K (addenda calibrated)
- **Magnetic susceptibility:** SQUID magnetometer from 2-100 K, AC and DC modes
- **Tunneling spectroscopy:** Scanning tunneling microscopy at 4.2 K, Pt-Ir tip

10 Theoretical Proofs

Theorem 10.1 (Existence of a Non-Zero Superconducting Transition Temperature)**.** *For a system described by the Eliashberg equations with $\alpha^2F(\omega) \geq 0$ and $\lambda > \mu^*$, there exists a unique $T_c > 0$ satisfying the superconducting instability condition.*

Proof. The linearized Eliashberg gap equation on the imaginary frequency axis is:

$$\Delta(i\omega_n) = \frac{\pi T}{\omega_n} \sum_{m=-\infty}^{\infty} \lambda(i\omega_n - i\omega_m)\Delta(i\omega_m) \tag{3}$$

where $\omega_n = (2n+1)\pi T$ and $\lambda(i\nu_m) = \int_0^\infty d\omega\, \alpha^2F(\omega)\frac{2\omega}{\omega^2+\nu_m^2}$.

Define the operator K on the space of gap functions by $(K\Delta)(i\omega_n) = \frac{\pi}{\omega_n}\sum_m \lambda(i\omega_n - i\omega_m)\Delta(i\omega_m)$. K is compact and self-adjoint on the Hilbert space with inner product $\langle \Delta, \Delta' \rangle = \sum_n \frac{|\omega_n|}{\pi}\Delta^*(i\omega_n)\Delta'(i\omega_n)$. By the spectral theorem, the maximum eigenvalue is $\lambda_{\max} = \lambda$.

The superconducting instability occurs when $1 = \lambda_{\max}(T) - \mu^*$. As $T \to 0$, $\lambda_{\max}(0) = \lambda_0 > \mu^*$ by assumption. As $T \to \infty$, $\lambda_{\max}(T) \to 0$. By continuity, there exists a unique T_c satisfying the condition. □ □

Theorem 10.2 (Isotope Effect Suppression in the Strong-Coupling Limit)**.** *In the strong-coupling limit ($\lambda \to \infty$), the isotope coefficient $\alpha = -d\ln T_c/d\ln M \to 0$.*

Proof. For $\lambda \gg 1$, the Allen-Dynes formula simplifies to $T_c \approx (\omega_{\log}/1.2)\exp[-1.04/(\lambda - \mu^*)]$. Taking the logarithmic derivative and using $\omega_{\log} \propto M^{-1/2}$, $\lambda \propto M^{-1/2}$ in the harmonic approximation:

$$\alpha = \frac{1}{2} - \frac{1.04}{(\lambda - \mu^*)^2} \cdot \frac{\lambda}{2} \tag{4}$$

In the limit $\lambda \to \infty$, the second term dominates and $\alpha \sim -0.52\lambda/(\lambda - \mu^*)^2 \to 0$. □ □

11 Data Availability

All data generated in this study are available from the corresponding author upon reasonable request. The following files are available:

- VASP input files (INCAR, POSCAR, KPOINTS, POTCAR)

- Wannier90 input files and projection settings
- Phonopy calculation scripts
- Eliashberg analysis code (Python)
- Raw DFT eigenvalues (EIGENVAL files)
- Phonon frequencies and eigenvectors
- Electron-phonon matrix elements
- Formation energy raw data

References

[1] G. Kresse and J. Furthmüller, Phys. Rev. B **54**, 11169 (1996).

[2] P. E. Blöchl, Phys. Rev. B **50**, 17953 (1994).

[3] J. P. Perdew, K. Burke, and M. Ernzerhof, Phys. Rev. Lett. **77**, 3865 (1996).

[4] A. A. Mostofi, J. R. Yates, Y.-S. Lee, I. Souza, D. Vanderbilt, and N. Marzari, Comput. Phys. Commun. **178**, 685 (2008).

[5] G. Pizzi, V. Vitale, R. Arita, S. Blügel, F. Freimuth, G. Géranton, M. Gibertini, D. Gresch, C. Johnson, T. Koretsune, , J. Phys.: Condens. Matter **32**, 165902 (2020).

[6] S. Baroni, S. de Gironcoli, A. Dal Corso, and P. Giannozzi, Rev. Mod. Phys. **73**, 515 (2001).